

## From Scratch Closure to Electrolyte Barrier Restoration in Self-Healing Polyurethane Coatings

Montano, Vincenzo; Vogel, Wouter; Smits, Angela; Van Der Zwaag, Sybrand; Garcia, Santiago J.

**DOI**

[10.1021/acsapm.1c00323](https://doi.org/10.1021/acsapm.1c00323)

**Publication date**

2021

**Document Version**

Final published version

**Published in**

ACS Applied Polymer Materials

**Citation (APA)**

Montano, V., Vogel, W., Smits, A., Van Der Zwaag, S., & Garcia, S. J. (2021). From Scratch Closure to Electrolyte Barrier Restoration in Self-Healing Polyurethane Coatings. *ACS Applied Polymer Materials*, 3(5), 2802-2812. <https://doi.org/10.1021/acsapm.1c00323>

**Important note**

To cite this publication, please use the final published version (if applicable). Please check the document version above.

**Copyright**

Other than for strictly personal use, it is not permitted to download, forward or distribute the text or part of it, without the consent of the author(s) and/or copyright holder(s), unless the work is under an open content license such as Creative Commons.

**Takedown policy**

Please contact us and provide details if you believe this document breaches copyrights. We will remove access to the work immediately and investigate your claim.

# From Scratch Closure to Electrolyte Barrier Restoration in Self-Healing Polyurethane Coatings

Vincenzo Montano, Wouter Vogel, Angela Smits, Sybrand van der Zwaag, and Santiago J. Garcia\*

Cite This: *ACS Appl. Polym. Mater.* 2021, 3, 2802–2812

Read Online

ACCESS |



Metrics &amp; More



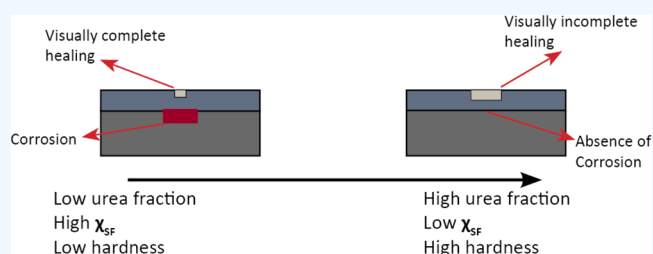
Article Recommendations



Supporting Information

**ABSTRACT:** The effects of the soft block fraction and H-bond state in thermoplastic polyurethanes on autonomous entropy-driven scratch closure and barrier restoration are studied. To this aim, comparable polyurethanes with different segmentation states are applied as organic coatings on plain carbon steel plates, scratched under very well-controlled conditions, and the scratch closure and sealing kinetics are studied in detail. The scratch closure is measured optically, while the barrier restoration is probed by the accelerated cyclic electrochemical technique (ACET). Scratch closure, attributed to entropic elastic recovery (EER), is followed in a marked two-step process by barrier restoration governed by local viscous flow and the state of the interfacial hydrogen bonding. Polyurethanes with a lower soft phase fraction lead to a higher urea/urethane ratio, which in turn influences the healing efficiency of each healing step. Interestingly, softer polyurethanes leading to efficient crack closure were unable to sufficiently restore barrier properties. The present work highlights the critical role of the soft/hard block and urea/urethane H-bond state content on crack closure and barrier restoration of anticorrosive organic coatings and points at design rules for the design of more efficient corrosion-protective self-healing polyurethanes.

**KEYWORDS:** self-healing polymer, self-healing coating, polyurethane, polymer architecture, urea, ACET



## 1. INTRODUCTION

The use of self-healing polymeric coatings has already been proposed for many years as a promising method for extending the lifetime of coated structures exposed to aqueous corrosion conditions.<sup>1–4</sup> The principal remaining challenge is to develop self-healing coatings with mechanical properties acceptable by industry such that, when damaged, they are able not only to close cracks but also to fully recover the original barrier function of the coating so that no preferential corrosion will take place at the former damage site. In extrinsic healing coatings, the damage restoration is due to the local flow and reaction of a liquid healing agent into the damage site as a result of the breakage of liquid-containing capsules dispersed in the coating. In intrinsic healing coatings, the design of the polymer macromolecule constituting the coating itself is responsible for the local on-demand mobility of the polymer network and damage restoration.

Intrinsic healing polymers offer the potential of healing large damages in corrosion-protective coatings. Such polymers owe their healing ability to the molecular design of the polymer network through the use of reversible chemical moieties that allow on-demand local temporary mobility of the network. To effectively exploit this characteristic in the field of coatings with the least human intervention possible, two things are required. First, a proper balance between elastic recovery after damage is required to bring the two crack planes in contact. Second, local viscous flow is required to allow for interface diffusion and

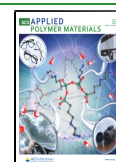
reaction to restore the barrier. The pressure-free scratch closure may be achieved by viscous flow or using so-called shape-memory principles to allow the mechanical closure of cracks by releasing the (elastic) energy stored during the damage.<sup>5</sup> This last concept is used in several intrinsic self-healing polymer coatings. In particular, from a polymer design point of view, the energy storage during damage leading to a shape-memory effect has been shown through the use of main chain entanglements, permanent cross-linking,<sup>6,7</sup> polymer blending,<sup>8,9</sup> and microphase separation.<sup>10,11</sup>

While the mechanical closure of cracks, which is relatively easy to monitor with conventional optical or SEM microscopy, is a prerequisite, the formation of entanglements and physical and chemical bonds at the polymer–polymer and polymer–metal interfaces are equally important from a corrosion protection perspective. These interfacial properties can be monitored using electrochemical techniques such as electrochemical impedance spectroscopy (EIS).<sup>4,12–15</sup> Quasi-autonomous crack closure in combination with interfacial healing may be hard to realize in a one-phase polymer system due to the

Received: March 9, 2021

Accepted: March 31, 2021

Published: April 13, 2021



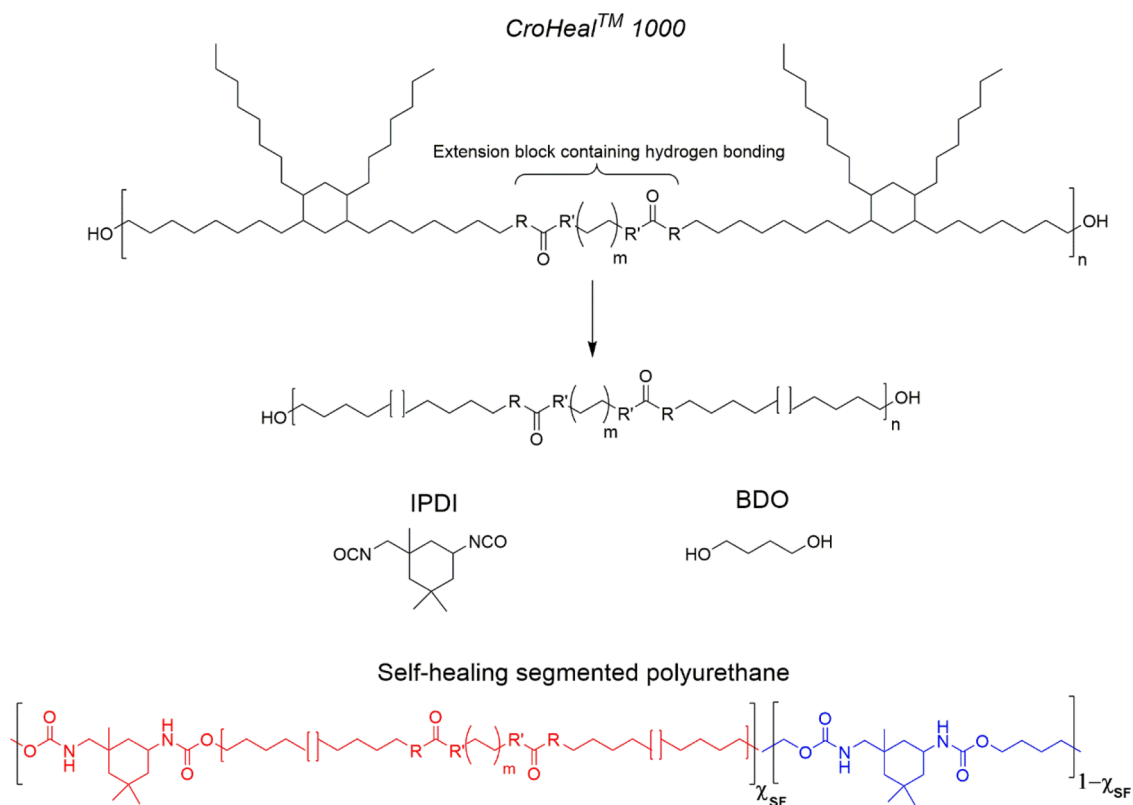


**Figure 1.** Monomers used (CroHeal 1000, IPDI, and BDO) and the segmented molecular structure of the synthesized polyurethanes as a function of the soft/hard block fraction ( $\chi_{SF}$ ). The red structure represents the nominal soft blocks, and the blue structure represents the hard blocks.

inherent dichotomy between fast chain interdiffusion (which guarantees rapid damage disappearance) and high binding energy of reversible moieties (which ensures high interfacial healing). To maximize the potential of the healing concept in protective coatings, it is necessary to control the polymer architecture and identify the polymer features that help to maximize both scratch closure and interfacial sealing. Earlier works showed that it is possible to control the mechanical properties of healed interfaces in branched polyurethanes by tuning the length of the dangling side chains<sup>16</sup> but also to quantify the relation between the content of reversible dynamic bonds and the work of deformation at healed interfaces through rheology deconvolution protocols.<sup>17</sup> Works on self-healing polyurethane coatings showed how their characteristic phase separation at the nanoscale induces delayed elasticity upon damage, driving the scratch closure process.<sup>18–20</sup> Nevertheless, there is no reported systematic work trying to unveil the role of the soft/hard block ratio on the different stages of the healing process in polyurethane coatings. To the best of our knowledge, this work presents the first systematic study to establish a relation between the soft/hard block ratio and H-bond state with the autonomous crack closure and barrier restoration.

The effect of hydrogen bonding on the interfacial healing of free-standing polymers has been reported many times. For comparable polymer networks, an increase in the content of dynamic hydrogen bonds and the use of hydrogen-bonding reversible moieties with higher binding energies (e.g., multi-dentate ligands) led to stronger healed interfaces when broken parts are manually brought in contact. The hydrogen-bonding functionality can be inferred from the reported dimerization constants calculated for several hydrogen-bonding groups

ranging from monodentate to quadruple bonding groups.<sup>21</sup> This idea has recently been intentionally exploited with well-selected monomers to increase the mechanical properties of intrinsic self-healing polymers,<sup>22</sup> but the positive effect of an increase in hydrogen-bonding binding energy on interfacial healing of polymers and coatings remains to be demonstrated.

In the present work, we investigate the effects of both the soft/hard block ratio and urea/urethane content on the healing process and efficiency of a set of self-healing polyurethanes with comparable chemistry and properties. By varying the ratio between a polyol with short aliphatic dangling chains, chain extender, and isocyanate, the degree of segmentation and soft phase fraction is controlled, and its impact on the balance between scratch closure and barrier restoration responsible for the passive corrosion protection functionality is investigated. The resulting polyurethane formulations are applied on carbon steel panels. As a result of the monomers used, the implemented strategy leads to a change in the relative ratio between urea (bidentate) and urethane (monodentate) reversible ligands. This allows insights into the effect of an increase in binding energy of the reversible group on both crack closure and crack sealing. FTIR was employed to quantify the urea/urethane content as a function of the soft fraction. Light optical microscopy and scanning electron microscopy allowed the monitoring and quantification of the crack closure process and kinetics. The accelerated cyclic electrochemical technique (ACET) is used to monitor the effect of the soft fraction and urea/urethane ratio on the barrier properties and sealing restoration after damage.

## 2. EXPERIMENTAL SECTION

**2.1. Materials.** Butyl acetate (BuAc, >99.7%), 1,4-butanediol (BDO, 99%), isophorone diisocyanate (IPDI, 98%), and dibutyltin dilaurate (DBDTL, 95%) were purchased from Sigma-Aldrich. The polyether siloxane copolymer wetting additive TEGO Wet 270 was purchased from Evonik Industries. Polyol CroHeal 1000 (equivalent molecular weight, 1200 g/mol) was kindly provided from Croda Nederland B.V. Sodium chloride was purchased from VWR International. All the reagents were used as received without further purification.

**2.2. Synthesis of Segmented Polyurethanes and Coating Preparation.** Six segmented polyurethanes were synthesized by a single-shot technique reacting IPDI (diisocyanate), BDO (chain extender), and CroHeal 1000 (polyol). The molecular structure of the segmented polyurethanes is shown schematically in Figure 1. The short hard segments (IPDI + BDO) are connected by long and highly aliphatic soft segments (IPDI + CroHeal 1000). The nominal molar soft phase fraction was estimated as  $\chi_{SF} = \frac{n(\text{CroHeal 1000})}{n(\text{CroHeal 1000}) + n(\text{BDO})}$ , where  $n$  stands for the number of moles.

The nominal soft phase fraction was controlled by varying the molar ratio CroHeal/BDO in the monomer feed yet maintaining the same isocyanate/hydroxyl functional group ratio (NCO/OH = 1.1). By this approach,  $\chi_{SF}$  was set to the following levels:  $\chi_{SF} = 0.71, 0.59, 0.51, 0.42,$  and  $0.27$ . Here, the synthesis of polymer  $\chi_{SF} = 0.42$  is reported in more detail as it is the representative of the synthesis process used for all polymer systems.

CroHeal 1000 was heated for 1 h at 60 °C to reduce the intrinsic viscosity of the polyol and facilitate mixing. Subsequently, 6.0 g (6.00 mmol) of CroHeal 1000 was transferred to a 20 mL polypropylene cup. Butyl acetate solvent (BuAc, 0.94 g, 8.13 mmol) was quickly added to further reduce the intrinsic viscosity. 1,4-Butanediol (0.6 g, 6.66 mmol) was then transferred to the cup. Subsequently, TEGO 270 (0.024 g) and dibutyltin dilaurate (DBDTL, 0.063 g, 0.1 mmol) were added dropwise. Immediately thereafter, isophorone diisocyanate (IPDI, 2.85 g, 12.82 mmol) was dosed using a syringe. The system was stirred vigorously using a mechanical agitator, and the reaction was left to proceed for 15 s at room temperature. The mixture was then applied on an acetone-cleaned carbon automotive steel plate (Q-panel) using a coating bar with a wet thickness of 150  $\mu\text{m}$ , leading to coatings with a dry thickness of  $100 \pm 5.0 \mu\text{m}$ . For bulk polymer characterization, a part of the polymer mixture was poured into a 4 × 4 cm PTFE mold to obtain free-standing films of  $1 \pm 0.2$  mm thickness. Analogous procedures were followed for the other polymers as detailed in the Supporting Information Table S1.

Both the coated panels and PTFE molds with the polymer mixtures were dried for 30 min at ambient laboratory conditions and subsequently cured for 30 min at 60 °C in an air-recirculating furnace. The polyurethane coatings and free-standing films were then equilibrated for at least 1 week at ambient laboratory conditions prior to testing.

**2.3. Characterization Methods.** **2.3.1. Attenuated Total Reflectance Infrared Spectroscopy (ATR-FTIR).** Attenuated total reflectance Fourier transform infrared spectroscopy was used to monitor synthesis completion and study the state of hydrogen bonding in the proposed segmented polyurethanes. Each analyzed ATR-FTIR spectrum, obtained with a PerkinElmer Spectrum 100, was the average of 32 scans over the wavenumber region 4000–500  $\text{cm}^{-1}$  with a resolution of 1  $\text{cm}^{-1}$ .

The infrared spectra were deconvoluted over the wavenumber range 1800–1600  $\text{cm}^{-1}$  to identify hidden subpeaks that give physical information on the state of the hydrogen bond of the carbonyl group (i.e., monodentate and bidentate hydrogen bonds related to urea and urethane groups, respectively). The subpeaks were identified by the analysis of the second-order derivatives of the infrared spectrum function. A fitting procedure was subsequently applied using Gaussian functions centered at the wavenumber corresponding to the local minima of the second-order derivative. The fitting procedures were performed using the software OriginPro 2015 (OriginLab). For all

polymers, the coefficients of determination ( $r^2$ ) were higher than 0.99, indicating a high fitting reliability.

It should be noted that the insufficient solubility of the polymers ( $\ll 1$  mg/mL) in the available elution solvents (tetrahydrofuran, *n*-methyl-2-pyrrolidone, deuterated chloroform  $\text{CDCl}_3$ , and deuterated dimethyl sulfoxide  $\text{DMSO-}d_6$ ) did not allow for appropriate gel permeation chromatography (GPC) or nuclear magnetic resonance (NMR) experiments.

**2.3.2. Accelerated Cyclic Electrochemical Technique (ACET).** The ACET measurements were performed at room temperature following well-established procedures.<sup>23,24</sup> The tests were performed with an Autolab PGSTAT 302N potentiostat/galvanostat using a conventional three-electrode cell configuration consisting of a saturated Ag/AgCl reference electrode, a carbon black rod with a diameter of 50 mm as a counter electrode, and a coated carbon steel substrate as a working electrode. A volume of 50 mL of stagnant 0.5 M NaCl aqueous solution in equilibrium with air was used as electrolyte. The samples were placed vertically in the electrochemical cell with an exposed area of around 0.8  $\text{cm}^2$ . This geometry allowed monitoring the sample under immersion during the whole duration of the test with a CCD camera as performed elsewhere.<sup>25</sup> A Faraday cage was employed to avoid the interference of external electromagnetic fields. The intact and healed coating systems were electrochemically characterized *in duplo*, showing good reproducibility.

Prior to the test, the open-circuit potential (OCP) of the samples was measured and used for the first electrochemical impedance spectroscopy (EIS) test. At this moment, the testing procedure consists of the repetition of three consecutive steps: (i) a nondestructive EIS at 10 mV (rms) sinusoidal perturbation with respect to the OCP in the frequency range  $10^{-1}$ – $10^4$  Hz (10 data points per frequency decade were acquired), (ii) a cathodic polarization at a constant potential of  $-4$  V for 20 min, and (iii) a potential relaxation for 3 h to record the open-circuit potential (OCP) evolution with time. The test sequence was repeated for five times.

**2.3.3. Calculations of Coating Capacitance.** The coating capacitance was calculated directly from the EIS data using eq 1:

$$C_c = \frac{1}{2\pi f_i Z''} \quad (1)$$

where  $f_i$  is the excitation frequency and  $Z''$  is the imaginary part of the impedance at the  $f_i$  excitation frequency.  $f_i$  was set at 230 Hz, where the total impedance of all systems is entirely dominated by the polymer capacitance and without external interferences.<sup>26–28</sup>  $C_c$  is a direct estimation of the water uptake considering the relation:

$$C_c = \epsilon \epsilon_0 \frac{A}{d} \quad (2)$$

where  $\epsilon$  is the dielectric constant of the coating,  $\epsilon_0$  is the vacuum permittivity,  $A$  is the area of the coating exposed to the electrolyte, and  $d$  is the coating thickness. As the coating absorbs water, the dielectric constant of the coating increases and with it the coating capacitance.

**2.3.4. König Hardness Measurements.** König hardness measurements were performed using the Pendule Persoz & König Model 3034 No. 95-001 manufactured by Braive Instruments operating at 220 V and 50 Hz following ISO 1522. Glass-coated panels (7 × 20 cm) with an average thickness of 120  $\mu\text{m}$  were tested.

**2.3.5. Creation of Scratch Damage.** Scratches of 5 mm in length and 100  $\mu\text{m}$  in width were produced at  $T = 21$  °C by a computerized scratch machine, the CSM Instrument Scratch Tester, using a fresh razor blade with a 100  $\mu\text{m}$  wide tip until the razor blade tip reached the steel substrate. To do so, the axial force was varied between a minimum of 1 N ( $\chi_{SF} = 0.71$ ) and a maximum of 1.8 N ( $\chi_{SF} = 0.27$ ), depending on the hardness of the coating. The sliding speed was set to 1 mm/min, and the tip-to-metal contact was monitored with an LED.

**2.3.6. Scanning Electron Microscopy.** A high-resolution JEOL SEM (JSM-75000F) operating at 5 kV was employed to visualize the degree of scratch closure at the end of the healing process. To do this,

the polymer coatings were subjected to a high-vacuum, gold sputtering treatment before observation. Since gold sputtering was required for samples to be observed, every data point shown in the closure kinetics study corresponds to a different coating specimen.

**2.3.7. Thermal Analyses.** Thermal properties were determined by thermogravimetric analysis (TGA) and differential scanning calorimetry (DSC). TGA analyses were performed from room temperature to 600 °C under a dry nitrogen atmosphere at a 10 °C/min heating rate using a PerkinElmer TGA 4000. DSC measurements were performed under a dry nitrogen atmosphere and 10 °C/min heating and cooling rates over the temperature range -40 to 200 °C using a PerkinElmer Pyris Sapphire DSC. The glass transition temperature ( $T_g$ ) was determined using the inflection point method.

**2.3.8. Melt Rheology.** Oscillatory shear experiments were carried out on a strain-controlled Physica MCR 102 (Anton Paar GmbH) rheometer using a parallel plate geometry. The diameter of the plate was 8 mm, and the sample thickness was set to  $1.0 \pm 0.2$  mm. Temperature sweep analyses were carried out over the temperature range -20 to 180 °C using a heating rate of 2.8 °C/min. All the tests were run at a fixed strain of  $\gamma = 0.1\%$ , which is always within the linear viscoelastic regime as established by preliminary strain amplitude analyses.

**2.3.9. X-ray Diffraction Analysis.** Room-temperature X-ray diffraction (XRD) spectra of the polymers deposited on aluminum holders were recorded using a Rigaku MiniFlex 600 diffractometer. The angle ranged from  $2\theta = 1$  to  $60^\circ$  with  $0.1^\circ$  increments. The samples were rotated during the measurement in an evacuated vacuum chamber.

### 3. RESULTS AND DISCUSSION

**3.1. Effect of the Soft Phase Fraction on the Polymer Structure and Dynamics.** Segmented polyurethanes (TPU) are well-known for their characteristic nanophase-separated morphology, which determines their rubber-like properties (e.g., rubbery elasticity). The phase separation at the nanoscale is attributed to the presence in the main chain of short hydrophilic blocks (the hard block) connected by long hydrophobic segments (the soft block). The block-like molecular structure of the segmented polyurethanes presented in this manuscript is shown in Figure 1. Short blocks with strong hydrogen bonds (IPDI and BDO) are connected by long hydrophobic segments (IPDI + CroHeal 1000). As a result, when less CroHeal1000 is used (less  $\chi_{SF}$ ), the polymer becomes more segmented with longer hard blocks within the random character of the polymers.

All polymers are partially hazy, with a glass transition ( $T_g$ ) located between 4 °C ( $\chi_{SF} = 0.71$ ) and 27 °C ( $\chi_{SF} = 0.27$ ) as determined by DSC (Figure S2 and Table S2). Independently of the  $\chi_{SF}$ , all polymers show an equally high temperature stability with 5% weight loss at temperatures higher than 300 °C (Table S2).

Given the monomers used and the resulting bonds, the polymers used in this work are expected to have both monodentate (urethane) and bidentate (urea) groups in the polymer network. The formation of urea linkages is determined by a simple chemical process: in poly(urea)-urethanes, the urea linkages can be formed due to the reaction with moisture. In this particular case, a part of the isocyanate groups of IPDI can react with water molecules to give carbamic acid groups that decompose into amines and  $\text{CO}_2$ ; the amines will subsequently react with another isocyanate group to form a urea bond. Due to the large steric hindrance of CroHeal 1000 polyol, the free IPDI preferentially reacts with BDO to form urethane bonds. Some of these subsequently react with the

amines resulting from the side reaction between IPDI and moisture to form urea bonds.

In view of the difference in binding energy between the two ligands and its potential impact on interfacial healing, we quantified the relative ratio between urea and urethane ligands with an FTIR deconvolution protocol.<sup>29,30</sup> The IR study focuses on the amide group ( $-\text{NH}-\text{C}=\text{O}-$ ) configuration. As a first step, the second derivative of the IR spectrum for the amide I carbonyl (the amide carbonyl of urethane or urea moieties) stretching vibration region of interest ( $1800-1640 \text{ cm}^{-1}$ ) was calculated and all the sub-bands were identified (Figure 2A shows the example for three compositions). This

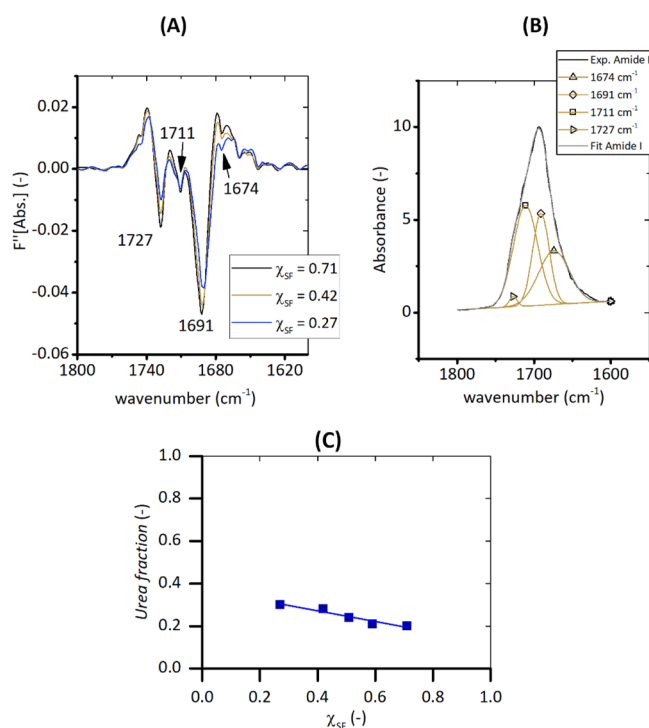


**Figure 2.** Quantification of urea and urethane groups from FTIR deconvolution. (A) Second derivative plots of ATR-FTIR spectra of  $\chi_{SF} = 0.71, 0.42,$  and  $0.27$  showing the presence of four local minima in the amide I band. (B)  $\chi_{SF} = 0.27$  amide I deconvolution. (C) Evolution of the Urea fraction as a function of the  $\chi_{SF}$ .

process revealed the presence of four peaks hidden in the carbonyl region. Based on previous reports on segmented polyurethanes<sup>30</sup> and theory on the bond vibration strength (higher strength leads to lower wavenumbers), the peaks were identified as free carbonyl groups ( $1727 \text{ cm}^{-1}$ ), disordered hydrogen-bonded urethane carbonyl ( $1711 \text{ cm}^{-1}$ ), ordered hydrogen-bonded urethane carbonyl ( $1694 \text{ cm}^{-1}$ ), and hydrogen-bonded urea groups ( $1671 \text{ cm}^{-1}$ ). The same principal sub-bands were found for all the polyurethanes studied here (see the Supporting Information Figure S8).

With the peaks identified, the deconvolution of the IR spectrum was performed by running a mean square minimization fitting procedure to optimize the fit for the amide I experimental IR curve using four time constants. The results of the fitting procedure for  $\chi_{SF} = 0.27$  are shown in Figure 2B. For all polymers, the correlation coefficient was higher than 0.99, which confirms the very good agreement between fitness and experimental functions. With the fit complete, the area under each single Gaussian subpeak was

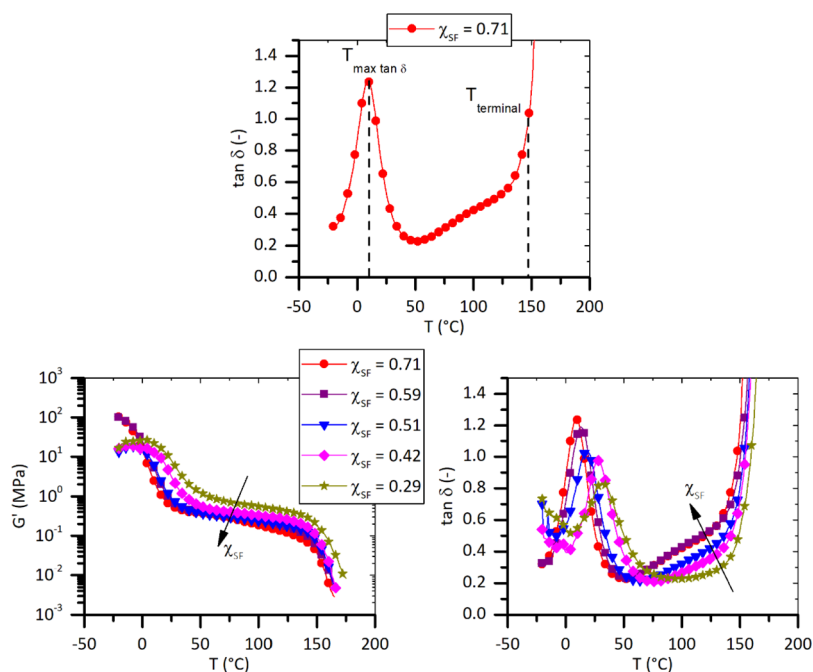


**Figure 3.** Oscillatory shear analysis results. The viscoelastic behavior resembles the typical one of segmented polyurethanes. The increase of  $\chi_{SF}$  determines a faster access to terminal relaxation, an increase of dissipation in the apparent-plateau region, and a higher damping at glass transition.

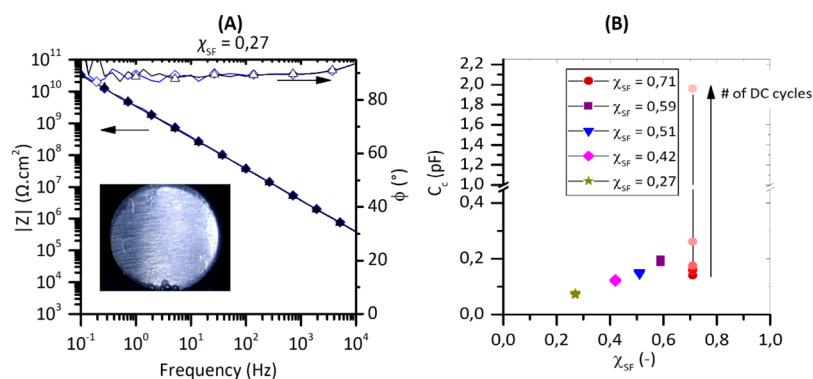
integrated to obtain quantitative information about the distribution of the hydrogen bond state. For  $\chi_{SF} = 0.27$ , a very low fraction of free carbonyl groups (non-hydrogen-bonded) was obtained as can be inferred from the small area under the free carbonyl sub-band ( $1727\text{ cm}^{-1}$ ). Urethane ( $1711$  and  $1691\text{ cm}^{-1}$  sub-bands) and urea hydrogen-bonded carbonyls ( $1674\text{ cm}^{-1}$ ) appear as equally concentrated. The fitting procedure was applied to all coating formulations with comparable conclusions as shown in Table S3 and Figure S8.

Figure 2C shows the Urea fraction dependency with the  $\chi_{SF}$  (blue square data points). The Urea fraction was calculated using the quantitative data obtained by the FTIR deconvolution fitting as:

$$\text{Urea fraction} = \frac{IA_{\text{urea}}}{IA_{\text{urea}} + IA_{\text{ord.urethane}} + IA_{\text{disord.urethane}}} \quad (3)$$

where  $IA_{\text{urea}}$ ,  $IA_{\text{ord.urethane}}$ , and  $IA_{\text{disord.urethane}}$  are the integrated areas under the deconvoluted urea, ordered urethane, and disordered urethane IR peaks, respectively. As can be seen, the Urea fraction decreases linearly with the increase of soft block fraction  $\chi_{SF}$  from values  $>0.3$  for the most segmented polyurethane ( $\chi_{SF} = 0.27$ ) to about 0.19 for the least-segmented polyurethane ( $\chi_{SF} = 0.71$ ). The increase in Urea fraction with the decrease of  $\chi_{SF}$  is simply explained by looking at the monomer feed for the different formulations. Since BDO has a much lower molecular weight compared to CroHeal 1000, to keep the ratio OH/NCO constant ( $\text{OH/NCO} = 1.1$ ), a higher IPDI molar content is fed for the polymer designed with low  $\chi_{SF}$ . As explained, the reaction between IPDI and moisture gives rise to amines in the mixture, which then lead to the formation of urea linkages. Therefore, the higher IPDI molar content justifies the higher fraction of urea units in the final network. This confirms the influence of soft/hard phase ratio on the presence of high energetic bidentate reversible groups.

The differences in the polymer architecture due to the variation of the soft phase fraction can be found back in the macromolecular dynamics of the networks, as demonstrated through oscillatory shear experiments. Figure 3 presents the small-amplitude, temperature-sweep shear tests for all the synthesized polymers. The elastic data are presented as elastic shear modulus ( $G'$ ) as a function of temperature. The viscoelastic data are reported in the form of the tangent of the phase angle (damping factor,  $\tan \delta = G''/G'$ ) to quantify the ratio between the energy lost and energy stored,<sup>31</sup> particularly relevant during a relaxation transition. Following the temperature dependence of  $\tan \delta$ , it can be inferred that the viscoelastic behavior indeed resembles that of segmented polyurethanes. In this framework, the first dynamic transition at  $T_{\max \tan \delta}$  is attributed to the relaxation of the continuous soft matrix, while the next transition is associated with the presence of segregated hard segments, which are able to store mechanical energy for a broad range of temperatures until terminal relaxation occurs ( $T > T_{\text{terminal}}$ ). By decreasing the soft phase fraction  $\chi_{SF}$ , three effects are apparent: (i) in analogy with results on  $T_g$  obtained via calorimetry,  $T_{\max \tan \delta}$  (which is used as an alternative mechanical definition of the glass transition) shifts upward from  $9\text{ }^\circ\text{C}$  (for  $\chi_{SF} = 0.71$ ) to  $31\text{ }^\circ\text{C}$  (for  $\chi_{SF} = 0.27$ ); (ii) more segmented/harder (low  $\chi_{SF}$ ) polymers show delayed access to terminal relaxation ( $T_{\text{terminal}}$ ) and a decrease of the absolute value of  $\tan \delta$  in the plateau region ( $T_{\max \tan \delta} < T < T_{\text{terminal}}$ ), indicating a more efficient energy storage that can be attributed to the higher hard block fraction and nanophase segregation; and (iii) as expected for the lower amount of energy-dissipating blocks, lower  $\chi_{SF}$  leads to a decrease in damping at  $T_{\max \tan \delta}$  (lower  $\tan \delta$ ) because a lower fraction of the material is relaxing at the glass transition temperature. Similar effects were observed in earlier studies on segmented polyurethanes by Ferguson et al.<sup>32</sup> in which the polymer structure was systematically controlled by changing the amount of chain extender used.



**Figure 4.** Barrier properties of the intact coatings. (A) Bode plot showing the EIS results as a function of the ACET cycles for the sample  $\chi_{SF} = 0.27$ . The blue diamond markers show the initial EIS results (prior to any direct polarization). The black triangle markers show the final EIS (upon the fifth polarization cycle). Filled markers refer to the total impedance  $|Z|$ ; open markers refer to the phase  $\phi$ . The inset shows a photograph of the coating under immersion during the last ACET cycle. (B) Coating capacitance evolution with the polymer soft phase fraction  $\chi_{SF}$  and polarization cycles. Note that the coating capacitance increases with the polymer soft phase fraction  $\chi_{SF}$ .

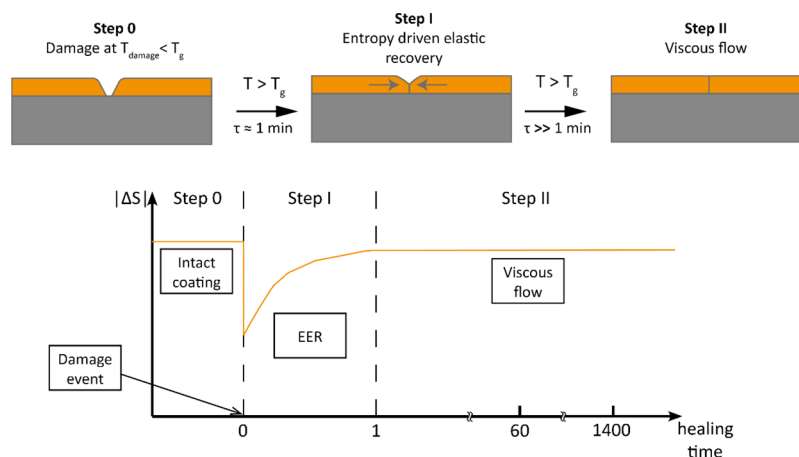


**Figure 5.** Schematic representation of entropy storage evolution in time in a damage and healing process at  $T_{\text{damage}} < T_g$  and  $T_{\text{healing}} > T_g$ .

**3.2. Effect of the Soft Phase Fraction on Barrier and Mechanical Properties of Intact Coatings.** Figure 4A shows a Bode plot with the EIS results obtained from the ACET test for an intact sample  $\chi_{SF} = 0.27$  as a function of the number of ACET cycles. The inset shows an optical snapshot of the sample obtained after the last ACET cycle to demonstrate the absence of defects. The Bode plot resembles that of a perfect capacitor (frequency independent phase  $\phi \approx 90^\circ$ ) characteristic of intact barrier coatings. The high impedance and phase angle and the absence of defects are maintained during the whole duration of the ACET test, i.e., there is no substantial difference between the first cycle (blue diamond markers) and the last cycle (black triangle markers). In agreement with previous work using this technique for intact coatings, the high stability of the EIS signal and absence of blisters with the cycles despite the strong polarization ( $-4$  V) are indications of the system being a coating with a low permeability, no manufacturing defects, and a strong adhesion.

To obtain a relation of the water uptake as a function of the polarization cycles and the soft block fraction, the coating capacitance ( $C_c$ ) was extrapolated using eq 1. Figure 4B shows the capacitance results for all the coating formulations and cycles. As can be seen, the coating capacitance  $C_c$  and, therefore, water uptake increase with the soft fraction ( $\chi_{SF}$ ) content, which in turn corresponds to a lower urea/urethane fraction. A similar trend was observed in a previous study<sup>33</sup>

using segmented hybrid poly(urea)urethanes in which a higher urea/urethane content led to a lower water uptake. Figure 4B also shows how the coatings maintain a similar coating capacitance throughout the ACET cycles. The highest soft fraction ( $\chi_{SF} = 0.71$ ) represents an exception to these trends, as this sample shows an initially lower coating capacitance than expected and an increase in the coating capacitance between the third and fifth DC cycles. This suggests that when the fraction of the soft phase is clearly higher than that of the hard block, the hydrophobic character of the polyol monomer dictates the initial degree of water permeability. The effect is nevertheless lost with the polarization cycles as, once the water ingresses, the resistance to absorb water decreases due to the lower amount of physical cross-links (hard blocks) to refrain the polymer from adapting to more water ingress. The trend of the coating capacitance with the cycles for each sample can be seen in Figure S3 of the Supporting Information.

A König hardness pendulum test was used to assess the coating mechanical properties. The results reported in Table S4 show a strong increase in König hardness when the soft phase fraction  $\chi_{SF}$  is decreased (e.g., from  $22.5 \pm 2.5$  s for  $\chi_{SF} = 0.71$  to  $130 \pm 5$  s for  $\chi_{SF} = 0.27$ ). This is in good agreement with the increase of the Urea fraction and segmentation observed in IR spectroscopy and in line with the stress-strain results reported for comparable polymers.<sup>17</sup>

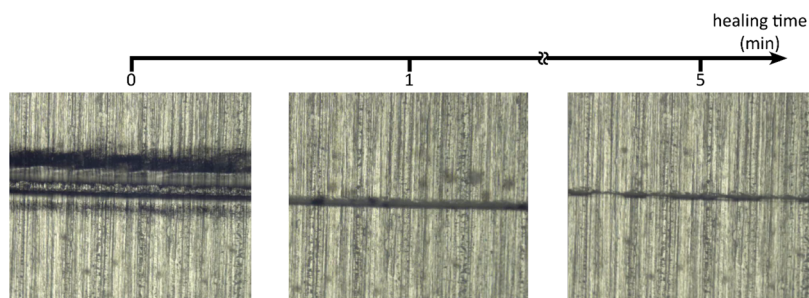


**Figure 6.** Time evolution of the healing process of  $\chi_{\text{SF}} = 0.42$  using snapshots of the video footage shown in the Supporting Information. At healing time = 0, the scratch is fully open and the metal substrate is clearly visible in between the two scratch fronts. At healing time = 1 min, the EER process is fully exploited and it brings the scratch fronts back to contact. At healing time = 5 min, viscous flow largely takes place as evidenced by bridging and (partial) scar disappearance.

### 3.3. Effect of the Soft Phase Fraction on Scratch Closure Kinetics.

The scratch-healing mechanism of the polyurethane coatings can be visualized by considering the thermodynamic response of the polymer to the mechanical damaging and healing events. Figure 5 schematizes the evolution of the local entropy density near the crack with time during a classical coating damage/healing process. When scratched by a razor blade at a temperature below the glass transition temperature ( $T_{\text{damage}} < T_g$ ), the actual cutting not only produces a scratch extending to the metallic substrate but also displaces the polymer in a lateral direction perpendicular to the scratch. This induced deformation produces an abrupt decrease in the system entropy near the damage. This change in local entropy is quasi-permanent due to the stable segregated phase that provides stable physical cross-link points that prevent the rapid network relaxation. This leads to entropy-driven energy storage at the damage location. Highly elastic polymer networks with high amounts of physical cross-link points are, in theory, able to store more entropy-driven energy. Upon heating at  $T_{\text{healing}} > T_g$ , the entropic energy stored during mechanical damage is released in a process known as entropy-driven elastic recovery (EER). This allows the displacement of the two sides of the damage toward the crack center. If this EER is sufficient, the two sides of the scratch will re-establish physical contact, and a healing interface will be formed to allow for the reshuffling of built-in reversible moieties. In case the polymer is scratched at a temperature above the glass transition temperature ( $T_{\text{damage}} > T_g$ ), no significant storage of entropic energy is expected since the polymer relaxes right after the creation of damage.

The scratch front displacement and kinetics of the process are functions of the characteristic network. After the EER, longer times at  $T_{\text{healing}} > T_g$  lead to no significant variation in entropy, while the system is energetically driven to viscous flow, which ultimately can lead to complete scar disappearance. The mechanism, here explained in thermodynamic terms, is known in literature as shape-memory-assisted self-healing (SMASH).<sup>8</sup>

In the current work, all the polymers were damaged at room temperature ( $T_{\text{damage}} = 21\text{ }^\circ\text{C}$ ), which is well above  $T_g$  for systems with  $\chi_{\text{SF}} = 0.71, 0.59,$  and  $0.51$ . In agreement with the theory described above, no entropy-driven scratch closure could be captured in these systems during the post-scratching optical observations as crack closure happened almost immediately after scratching. The other two samples,  $\chi_{\text{SF}} = 0.42$  and  $0.27$ , were damaged at  $T_{\text{damage}} < T_g$  and did show EER at the healing temperature. Figure 6 shows the process for  $\chi_{\text{SF}}$

$= 0.42$  at  $T_{\text{healing}} = 65\text{ }^\circ\text{C}$  with photo snapshots: start at 0 min, end of the EER process at  $\approx 1$  min, and viscous flow leading to scar disappearance at  $\approx 5$  min. A video footage recording of the first 5 min for this sample is available in the Supporting Information.

The quantification of the crack closure at the end of the healing process was performed using scanning electron microscopy (SEM). The micrographs for all compositions are shown in Figure S6. Figure 7 shows the quantified

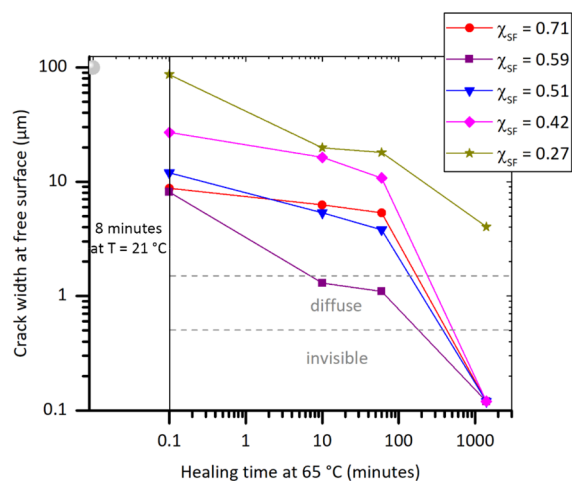


**Figure 7.** Scanning electron microscopy monitoring of crack closure. All the coatings were damaged with a razor blade tip ( $\approx 100\text{ }\mu\text{m}$  width). As a result, the initial damage width in all cases was  $100\text{ }\mu\text{m}$  as indicated by the gray ball. As the SEM sample preparation process takes time, the first healing time (healing time 0.1) was obtained after 8 min at  $T = 21\text{ }^\circ\text{C}$ . The gray lines named "invisible" and "diffuse" refer to the optical perception of the state of the scratch closure.

evolution of the crack width at the top surface of the coating as a function of the healing time at  $T_{\text{healing}} = 65\text{ }^\circ\text{C}$ . It should be noted that there was a delay of 8 min at  $21\text{ }^\circ\text{C}$  between the damage event and first data point at  $65\text{ }^\circ\text{C}$  (heal time = 0.1 min). At the moment of the start of the healing process at  $T = 65\text{ }^\circ\text{C}$  (healing time = 0.1 min), the polyurethane coatings with dominant soft phase fractions ( $\chi_{\text{SF}} = 0.71, 0.59,$  and  $0.51$ ) show comparably low scratch widths, one order of magnitude lower, than the width of the razor blade (Figure 6). For these polymers,  $T_{\text{damage}} \geq T_g$ ; therefore, the entropy-driven elastic recovery occurred right after damage and before the moment of the actual optical observation. Since  $\chi_{\text{SF}} = 0.27$  was damaged at  $T_{\text{damage}} \ll T_g$ , the

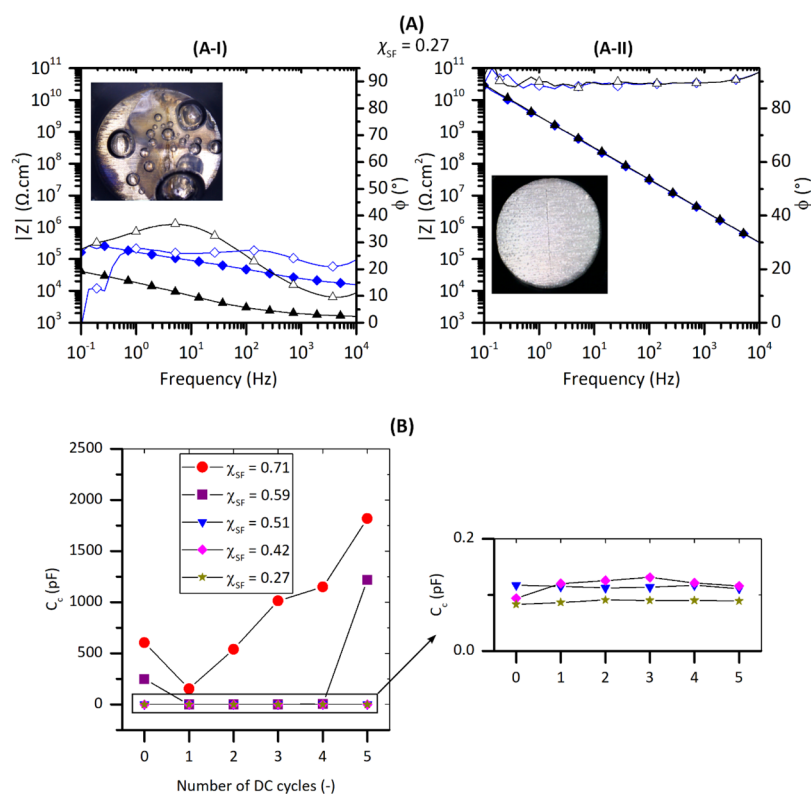


**Figure 8.** ACET results of healed PU coatings. (A-I) Bode plot of  $\chi_{SF} = 0.27$  tested in damaged condition (no healing treatment). (A-II) Bode plot of  $\chi_{SF} = 0.27$  tested after 60 min of healing at  $65^\circ\text{C}$ . (B) Coating capacitance evolution with number of polarization cycles during the ACET test for all TPU compositions. The insets in A-I and A-II are snapshots acquired at the end of the ACET tests.

stored entropy is high and the scratch width at the start of the healing process is very close to the width of the razor blade ( $\approx 100\ \mu\text{m}$ ). As expected,  $\chi_{SF} = 0.42$ , being damaged near its  $T_g$ , shows an intermediate behavior.

As can be seen, healing at  $65^\circ\text{C}$  induced a progressive scratch closure in all the polymers. At the end of the test (1400 min), all polymers show full crack closure (the scratches become invisible by SEM) except  $\chi_{SF} = 0.27$ , which needed more time to heal from its larger scratch width and showed full closure at 2800 min (not shown here). It is evident that the kinetics of scratch closure increase with the increase of the soft phase fraction. This result is in agreement with our observations on melt dynamics (Figure 3), which indicate a faster access to terminal relaxation when increasing  $\chi_{SF}$ .

**3.4. Effect of the Soft Phase Fraction on Barrier Restoration.** Besides scratch closure, the healing process of protective organic coatings must take into consideration the restoration of its original functionality as the barrier layer against the ingress of electrochemically active species. For convenience, the restoration of the barrier property is referred to as scratch sealing, while the physical disappearance of the scratch trace is referred to as scratch closure. For the present polyurethane, the two healing stages (closure and sealing) are decoupled.

Figure 8 shows the results of the electrochemical analysis of  $\chi_{SF} = 0.27$  when tested in two distinct conditions: (i) damaged (at room temperature, below  $T_g$ ) (Figure 8A-I) and (ii) after 60 min healing at  $65^\circ\text{C}$  (Figure 8A-II). As a result of the presence of the scratch, the coating offers no barrier to the electrolyte as seen in the total impedance similar to that of bare steel and a phase angle much lower than that for a pure capacitor (Figure 8A-I, blue diamond markers). Right after the

first polarization, the coating fails even further, showing processes compatible with cathodic debonding and gas evolution induced during the ACET test as clearly visible in the snapshots taken during the immersion with the CCD camera (insets of Figure 8A-I).

The ACET results for a sample with the same composition and damage but healed for 1 h at  $65^\circ\text{C}$  are radically different as seen in Figure 8A-II. Despite the crack seemingly not being fully closed (Figure 7 points at a residual crack width at a free surface of  $\approx 20\ \mu\text{m}$ ), the EIS signals suggest a complete recovery of the damage from an electrochemical perspective (full capacitive recovery), which is maintained with increasing number of polarization cycles. Similar results were obtained for most of the other polyurethane systems studied here.

To obtain a quantification of the degree of restoration of the barrier properties and to be able to compare the scratched-and-healed coatings with intact coatings of the same composition, the coating capacitances of the healed coatings were calculated from the EIS data in a similar way as for the intact coatings and are reported in Figure 8B. For coatings with high segmentation ( $\chi_{SF} = 0.51$ , 0.42, and 0.27), the barrier properties are completely restored to values comparable to the intact coatings ( $C_c < 0.2$  pF). Moreover, the *in situ* imaging showed no degradation signals at the healed scar during the whole duration of the ACET test, suggesting that the scratches are fully sealed, at least for a significant amount of time.

On the other hand, the two polymers designed with the highest soft phase fraction ( $\chi_{SF} = 0.59$  and 0.71) show a substantial decrease in barrier functionality when compared to the intact coatings. For  $\chi_{SF} = 0.59$ , a high capacitance is already probed at the first EIS measurement, even before any polarization is applied. This suggests the presence of an

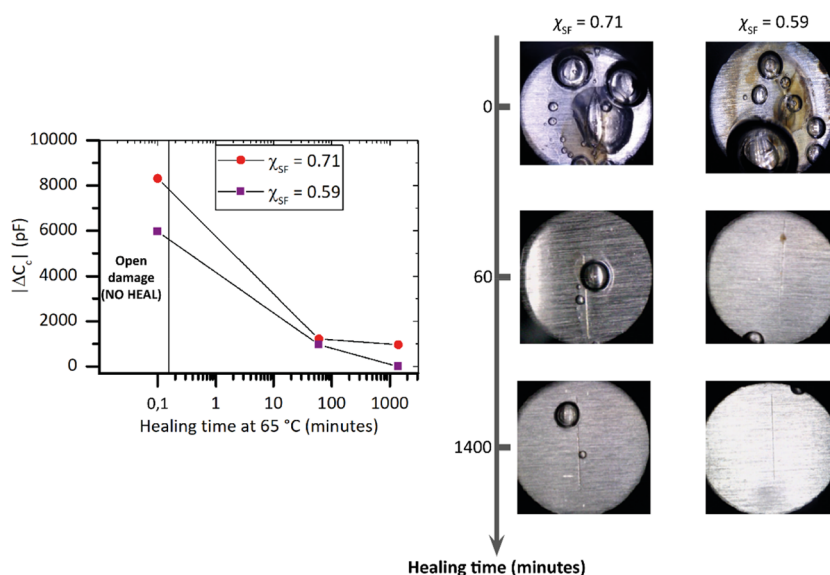


**Figure 9.** Effect of the healing time at 65 °C on the barrier property restoration for  $\chi_{SF} = 0.71$  and 0.59. Note that the data points plotted at healing time = 0.1 min correspond to an open damage (no healing) condition.

electrochemical path and therefore no full scratch sealing even though the crack width at the free surface is one order of magnitude smaller than that of the coatings with higher segmentation (2 vs 20  $\mu\text{m}$ , Figure 7). After the first polarization, the coating capacitance drops to values comparable to the intact coatings ( $C_c < 1$  pF) probably due to the water-induced closure of the damage through coating expansion, which can perfectly bridge 1  $\mu\text{m}$ . The high barrier functionality is kept intact for the subsequent cycles until, at cycle 5, the capacitance suddenly increases probably due to the reopening of the damage induced by the polarization events. Such a behavior has also been observed in other healing systems evaluated with this technique<sup>24</sup> and is in line with the delamination and significant oxide growth at the interface (inset in Figure 8B). Samples with  $\chi_{SF} = 0.71$  show an analogous behavior, although, in this case, the failure of the healed damage occurred already after the first polarization cycle showing a continuous increase of the capacitance with subsequent polarization cycles. Figure S12 shows the impedance and photographs before polarization and after cycle 5. The presence of two bubbles at the scratch during the first EIS suggests the incompleteness of the scratch closure, while the photograph after five cycles shows the same locations with bigger bubbles and delamination around the damage location, thereby confirming the indicated continued loss of barrier functionality.

The present results show that visual scratch closure does not necessarily lead to sealing (barrier restoration), but both are influenced by the characteristic soft phase fraction. The physical explanation for this behavior is discussed in Section 3.5. Good scratch sealing can be obtained with targeted soft phase fraction, fully recovering capacitance and related barrier performance.

As the coatings with the highest soft block ratio ( $\chi_{SF} = 0.71$  and 0.59) showed full scratch closure but incomplete barrier restoration, a detailed study of the effect of the healing time on sealing was performed. Figure 9 shows the results as the difference between the coating capacitance at cycles 0 and 5 (i.e.,  $|\Delta C_c| = |C_{C\_number\ of\ DC\ cycle = 0} - C_{C\_number\ of\ DC\ cycle = 5}|$ ) as a function of the healing time. The data points plotted at

healing time = 0.1 correspond to the as-damaged coatings. The results show how the sample  $\chi_{SF} = 0.59$  reaches high degrees of sealing after 1400 min of healing, proving that chain interdiffusion and randomization at the interface are time-dependent processes, even if the capacitance remains lower than that of the other samples. The sample with the highest soft block fraction on the other hand did not show any significant improvement when healing from 60 to 1400 min at 65 °C even if the crack optically has disappeared completely (see Figure 7). A possible explanation may reside in the low content of highly energetic urea bonds as will be discussed in Section 3.5.

**3.5. Physical Insights into Scratch Closure and Scratch Sealing.** As shown in Section 3.4, a complete crack closure estimated by optical analysis does not necessarily lead to the full recovery of the electrochemical barrier properties. This effect can be achieved when polymer diffusion and supramolecular reversible moiety reshuffling occur at the healed interface. The polymers used in this work contain two favorable features that promote interfacial healing: on the one hand, the effect of branch-mediated tube dilation to increase chain diffusion<sup>16</sup> and, on the other hand, the presence of dynamic hydrogen bonds (urethane and urea units), which assist the interfacial restoration. By combining all the results presented above, it becomes clear that polymers with a higher content of monodentate urethane linkages show faster scratch closure and damage optical disappearance (Figure 10A). This is due to the increase of mobility in the main chain induced by the decrease in reversible bond connectivity (lower energy is needed to break urethane units when compared to urea bonds). Moreover, the faster closure of the damage benefits from a higher main chain dilution effect due to the aliphatic side chains present in the soft segment. Nevertheless, the faster closure does not offset the beneficial effect that the reconstitution of highly energetic (bidentate) urea units has on the interfacial healing, as shown in Figure 10B. Figure 10C shows a schematic overview of the effect of the polymer architecture ( $\chi_{SF}$ ) and urea fraction on the two phenomena investigated (scratch closure and barrier restoration). The increase in the soft phase fraction leads to a larger scratch

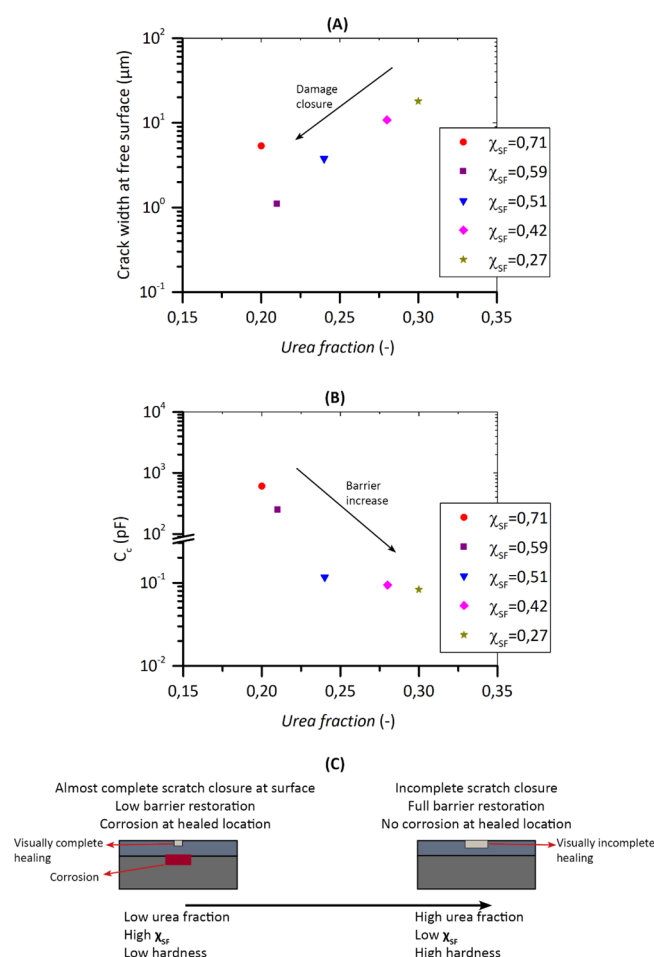


**Figure 10.** Effect of *Urea fraction* on self-healing of protective PU coatings. (A) Residual crack width at the free surface after 60 min of healing at 65 °C as measured by SEM as a function of the *Urea fraction*. (B) Coating capacitance as a measure of barrier against electrolyte permeation after 60 min of healing at 65 °C obtained after five polarization cycles in ACET. (C) Schematic representation of the effects of the polymer architecture ( $\chi_{SF}$ ) and urea fraction on scratch closure and barrier restoration after 60 min at 65 °C.

closure. Nevertheless, this increase in scratch closure does not correspond to a higher level of barrier restoration. The results may be explained by the energetic bonding energy of the involved dynamic groups. Since the urethane group is a monodentate group with an associative free energy of the hydrogen bond approximately 25% lower than that of urea units as obtained through quantum mechanical calculations,<sup>34</sup> higher contents of urea groups are expected to lead to a reduced segmental mobility at the healed interface. The restriction of interfacial mobility induced by the urea groups may be considered responsible for the drop in electrolyte diffusivity (barrier increase) in the systems with higher urea content despite lower through-thickness scratch closure. The results are in good agreement with previous reports on the interfacial mechanical restoration of poly(urea)urethane free-standing polymers containing high degrees of urea linkages<sup>35,36</sup> showing that, contrary to the general belief, softer coatings are not necessarily better than harder coatings in terms of overall healing performance when dealing with anticorrosive self-healing coatings, as barrier restoration is the dominant parameter.

## 4. CONCLUSIONS

The control of the soft phase fraction ( $\chi_{SF}$ ) in segmented polyurethanes is investigated as a design strategy to conjugate efficient scratch closure to high barrier restoration in anticorrosive barrier organic coatings. The kinetics of scratch closure accelerate with increasing soft phase,  $\chi_{SF}$ . This is in agreement with the observed faster terminal relaxation. However, high levels of scratch closure for high  $\chi_{SF}$  systems do not necessarily correspond to higher levels of barrier restoration as shown with electrochemical tests. More segmented coatings (lower  $\chi_{SF}$ ), on the other hand, show higher hardness and slower and, sometimes, even incomplete scratch closure at the coating surface but a more efficient sealing with high degrees of barrier restoration. This result is unexpected but very relevant as it sets a new but crucial design criterion for corrosion-protective and efficient self-healing organic coatings where optically detectable scratch closure cannot be directly related to restoration of the barrier functionality.

In the systems studied, the reduced amount of high energetic bidentate urea linkages in polymers with high soft phase fraction cannot guarantee an efficient and stable healed interface despite the more efficient scratch closure. High barrier restoration in the harder polymers may be attributed to the higher content of urea linkages leading to stronger interfacial bonds with restricted segmental mobility. The results moreover confirm that softer polymers with lower  $T_g$  do not necessarily lead to higher degrees of healing in anticorrosive polyurethane coatings since the overall performance at a healed damage is not governed by the scratch closure efficiency but by the barrier restoration.

## ■ ASSOCIATED CONTENT

### Supporting Information

The Supporting Information is available free of charge at <https://pubs.acs.org/doi/10.1021/acsapm.1c00323>.

Synthesis details, ATR-FTIR spectra and deconvolution results, König hardness, DSC and TGA thermograms, EIS/ACET spectra, SEM/EDX micrographs of scratch closure, XRD spectra (PDF)

Video of scratch closure (MP4)

## ■ AUTHOR INFORMATION

### Corresponding Author

**Santiago J. Garcia** – Novel Aerospace Materials group, Faculty of Aerospace Engineering, Delft University of Technology, Delft 2629 HS, The Netherlands; [orcid.org/0000-0002-2211-9972](https://orcid.org/0000-0002-2211-9972); Email: [s.j.garciaespallargas@tudelft.nl](mailto:s.j.garciaespallargas@tudelft.nl)

### Authors

**Vincenzo Montano** – Novel Aerospace Materials group, Faculty of Aerospace Engineering, Delft University of Technology, Delft 2629 HS, The Netherlands; [orcid.org/0000-0002-0002-3240](https://orcid.org/0000-0002-0002-3240)

**Wouter Vogel** – Croda, Coatings & Polymers business, Gouda 2802 BE, The Netherlands

**Angela Smits** – Croda, Coatings & Polymers business, Gouda 2802 BE, The Netherlands

**Sybrand van der Zwaag** – Novel Aerospace Materials group, Faculty of Aerospace Engineering, Delft University of Technology, Delft 2629 HS, The Netherlands

Complete contact information is available at:

<https://pubs.acs.org/10.1021/acsapm.1c00323>

## Notes

The authors declare no competing financial interest.

## ACKNOWLEDGMENTS

The authors acknowledge the financial support of Croda Nederland BV and the Dutch National Organization for Scientific Research, Domain Applied and Engineering Sciences (NWO-TTW) under grant number 15010.

## REFERENCES

- (1) García, S. J.; Fischer, H. R.; Van Der Zwaag, S. A Critical Appraisal of the Potential of Self Healing Polymeric Coatings. *Prog. Org. Coat.* **2011**, *72*, 211–221.
- (2) Stankiewicz, A.; Szczygiel, I.; Szczygiel, B. Self-Healing Coatings in Anti-Corrosion Applications. *J. Mater. Sci.* **2013**, *48*, 8041–8051.
- (3) Luo, X.; Mather, P. T. Shape Memory Assisted Self-Healing Coating. *ACS Macro Lett.* **2013**, *2*, 152–156.
- (4) Lutz, A.; Van Den Berg, O.; Van Damme, J.; Verheyen, K.; Bauters, E.; De Graeve, I.; Du Prez, F. E.; Terryn, H. A Shape-Recovery Polymer Coating for the Corrosion Protection of Metallic Surfaces. *ACS Appl. Mater. Interfaces* **2015**, *7*, 175–183.
- (5) Garcia, S. J. Effect of Polymer Architecture on the Intrinsic Self-Healing Character of Polymers. *Eur. Polym. J.* **2014**, *53*, 118–125.
- (6) Wang, Z.; Liang, H.; Yang, H.; Xiong, L.; Zhou, J.; Huang, S.; Zhao, C.; Zhong, J.; Fan, X. UV-Curable Self-Healing Polyurethane Coating Based on Thiol-Ene and Diels-Alder Double Click Reactions. *Prog. Org. Coat.* **2019**, *137*, 105282.
- (7) Gao, F.; Cao, J.; Wang, Q.; Liu, R.; Zhang, S.; Liu, J.; Liu, X. Properties of UV-Cured Self-Healing Coatings Prepared with PCDL-Based Polyurethane Containing Multiple H-Bonds. *Prog. Org. Coat.* **2017**, *113*, 160–167.
- (8) Rodriguez, E. D.; Luo, X.; Mather, P. T. Linear/Network Poly( $\epsilon$ -Caprolactone) Blends Exhibiting Shape Memory Assisted Self-Healing (SMASH). *ACS Appl. Mater. Interfaces* **2011**, *3*, 152–161.
- (9) Chen, T.; Fang, L.; Li, X.; Gao, D.; Lu, C.; Xu, Z. Self-Healing Polymer Coatings of Polyurea-Urethane/Epoxy Blends with Reversible and Dynamic Bonds. *Prog. Org. Coat.* **2020**, *147*, 105876.
- (10) Yarmohammadi, M.; Shahidzadeh, M.; Ramezanzadeh, B. Designing an Elastomeric Polyurethane Coating with Enhanced Mechanical and Self-Healing Properties: The Influence of Disulfide Chain Extender. *Prog. Org. Coat.* **2018**, *121*, 45–52.
- (11) Wang, Z.; Zhou, J.; Liang, H.; Ye, S.; Zou, J.; Yang, H. A Novel Polyurethane Elastomer with Super Mechanical Strength and Excellent Self-Healing Performance of Wide Scratches. *Prog. Org. Coat.* **2020**, *149*, 105943.
- (12) Samadzadeh, M.; Boura, S. H.; Peikari, M.; Ashrafi, A.; Kasirih, M. Tung Oil: An Autonomous Repairing Agent for Self-Healing Epoxy Coatings. *Prog. Org. Coat.* **2011**, *70*, 383–387.
- (13) Cho, S. H.; White, S. R.; Braun, P. V. Self-Healing Polymer Coatings. *Adv. Mater.* **2009**, *21*, 645–649.
- (14) González-García, Y.; García, S. J.; Hughes, A. E.; Mol, J. M. C. A Combined Redox-Competition and Negative-Feedback SECM Study of Self-Healing Anticorrosive Coatings. *Electrochem. Commun.* **2011**, *13*, 1094–1097.
- (15) García, S. J.; Fischer, H. R.; White, P. A.; Mardel, J.; González-García, Y.; Mol, J. M. C.; Hughes, A. E. Self-Healing Anticorrosive Organic Coating Based on an Encapsulated Water Reactive Silyl Ester: Synthesis and Proof of Concept. *Prog. Org. Coat.* **2011**, *70*, 142–149.
- (16) Montano, V.; Wempe, M. M. B.; Does, S. M. H.; Bijleveld, J. C.; van der Zwaag, S.; Garcia, S. J. Controlling Healing and Toughness in Polyurethanes by Branch-Mediated Tube Dilation. *Macromolecules* **2019**, *52*, 8067–8078.
- (17) Montano, V.; Senardi, M.; van der Zwaag, S.; Garcia, S. J. Linking Interfacial Work of Deformation from Deconvoluted Macro-

Rheological Spectrum to Early Stage Healing in Selected Polyurethanes. *Phys. Chem. Chem. Phys.* **2020**, *22*, 21750–21760.

(18) González-García, Y.; Mol, J. M. C.; Muselle, T.; De Graeve, I.; Van Assche, G.; Scheltjens, G.; Van Mele, B.; Terryn, H. A Combined Mechanical, Microscopic and Local Electrochemical Evaluation of Self-Healing Properties of Shape-Memory Polyurethane Coatings. *Electrochim. Acta* **2011**, *56*, 9619–9626.

(19) Jorcin, J.-B.; Scheltjens, G.; Van Ingelgem, Y.; Tourwé, E.; Van Assche, G.; De Graeve, I.; Van Mele, B.; Terryn, H.; Hubin, A. Investigation of the Self-Healing Properties of Shape Memory Polyurethane Coatings with the ‘Odd Random Phase Multisine’ Electrochemical Impedance Spectroscopy. *Electrochim. Acta* **2010**, *55*, 6195–6203.

(20) Chang, K.; Jia, H.; Gu, S. Y. A Transparent, Highly Stretchable, Self-Healing Polyurethane Based on Disulfide Bonds. *Eur. Polym. J.* **2019**, *112*, 822–831.

(21) Brunsveld, L.; Folmer, B. J. B.; Meijer, E. W.; Sijbesma, R. P. Supramolecular Polymers. *Chem. Rev.* **2001**, *101*, 4071–4098.

(22) Yanagisawa, Y.; Nan, Y.; Okuro, K.; Aida, T. Mechanically Robust, Readily Repairable Polymers via Tailored Noncovalent Cross-Linking. *Science* **2017**, *359*, 72–76.

(23) García, S. J.; Rodríguez, M. T.; Izquierdo, R.; Suay, J. Evaluation of Cure Temperature Effects in Cathodic Automotive Primers by Electrochemical Techniques. *Prog. Org. Coat.* **2007**, *60*, 303–311.

(24) Abdolaz Zadeh, M.; van der Zwaag, S.; Garcia, S. J. Assessment of Healed Scratches in Intrinsic Healing Coatings by AC/DC/AC Accelerated Electrochemical Procedure. *Surf. Coat. Technol.* **2016**, *303*, 396–405.

(25) Denissen, P. J.; Garcia, S. J. Cerium-Loaded Algae Exoskeletons for Active Corrosion Protection of Coated AA2024-T3. *Corros. Sci.* **2017**, *128*, 164–175.

(26) Walter, G. W. The Application of Impedance Spectroscopy to Study the Uptake of Sodium Chloride Solution in Painted Metals. *Corros. Sci.* **1991**, *32*, 1041–1058.

(27) Barranco, V.; Thiemann, P.; Yasuda, H. K.; Stratmann, M.; Grundmeier, G. Spectroscopic and Electrochemical Characterisation of Thin Cathodic Plasma Polymer Films on Iron. *Appl. Surf. Sci.* **2004**, *229*, 87–96.

(28) Barranco, V.; Carpentier, J.; Grundmeier, G. Correlation of Morphology and Barrier Properties of Thin Microwave Plasma Polymer Films on Metal Substrate. *Electrochim. Acta* **2004**, *49*, 1999–2013.

(29) Coleman, M. M.; Lee, K. H.; Skrovanek, D. J.; Painter, P. C. Hydrogen Bonding in Polymers. 4. Infrared Temperature Studies of a Simple Polyurethane. *Macromolecules* **1986**, *19*, 2149–2157.

(30) Mattia, J.; Painter, P. A Comparison of Hydrogen Bonding and Order in a Polyurethane and Poly(Urethane-Urea) and Their Blends with Poly(Ethylene Glycol). *Macromolecules* **2007**, *40*, 1546–1554.

(31) Ferry, J. D. *Viscoelastic Properties of Polymers*; Wiley, 1980.

(32) Ferguson, J.; Hourston, D. J.; Meredith, R.; Patsavoudis, D. Mechanical Relaxations in a Series of Polyurethanes with Varying Hard to Soft Segment Ratio. *Eur. Polym. J.* **1972**, *8*, 369–383.

(33) de Oliveira, M. C. L.; Antunes, R. A.; Costa, I. Effect of the NCO/OH Molar Ratio on the Physical Aging and on the Electrochemical Behavior of Polyurethane-Urea Hybrid Coatings. *Int. J. Electrochem. Sci.* **2013**, *8*, 4679–4689.

(34) Ylgör, E.; Ylgör, I.; Yurtsever, E. Hydrogen Bonding and Polyurethane Morphology. I. Quantum Mechanical Calculations of Hydrogen Bond Energies and Vibrational Spectroscopy of Model Compounds. *Polymer* **2002**, *43*, 6551–6559.

(35) Grande, A. M.; Garcia, S. J.; van der Zwaag, S. On the Interfacial Healing of a Supramolecular Elastomer. *Polymer* **2015**, *56*, 435–442.

(36) Feula, A.; Pethybridge, A.; Giannakopoulos, I.; Tang, X.; Chippindale, A.; Siviour, C. R.; Buckley, C. P.; Hamley, I. W.; Hayes, W. A Thermoreversible Supramolecular Polyurethane with Excellent Healing Ability at 45 °C. *Macromolecules* **2015**, *48*, 6132–6141.